crystals

MDPI

Article

Synthesis, Characterization and Catalytic Evaluation of Chromium Oxide Deposited on Titania–Silica Mesoporous Nanocomposite for the Ethane Dehydrogenation with CO_2

Abdulrhman S. Al-Awadi [1], Ahmed Mohamed El-Toni [2,*], Saeed M. Al-Zahrani [1], Ahmed E. Abasaeed [1] and Aslam Khan [2]

[1] Chemical Engineering Department, King Saud University, Riyadh 11421, Saudi Arabia; alawadi@KSU.EDU.SA (A.S.A.-A.); szahrani@ksu.edu.sa (S.M.A.-Z.); abasaeed@KSU.EDU.SA (A.E.A.)
[2] King Abdullah Institute for Nanotechnology, King Saud University, Riyadh 11451, Saudi Arabia; aslamkhan@ksu.edu.sa
* Correspondence: aamohammad@ksu.edu.sa

Received: 18 March 2020; Accepted: 4 April 2020; Published: 20 April 2020

Abstract: Ti modification of mesoporous silica support has been reported as an effective way to enhance Cr–Ti–Si interactions that, in turn, impact the catalytic dehydrogenation of ethane with CO_2. However, such modification necessitates a repeated, time-consuming and tedious process. In this work, a simple, fast and facile approach has been utilized to synthesize chromium-oxide-loaded titania–silica mesoporous nanocomposites. A series of Cr(y)/Ti(x)–Si mesoporous nanocomposite catalysts with varying Ti and Cr contents were prepared and tested in the dehydrogenation of ethane with carbon dioxide. The as-synthesized catalysts were characterized by XRD, TEM, SEM, BET, UV–Vis–DR, XPS and H_2–TPR techniques. The effect of titanium content, as well as chromium loading on the performance of the prepared Cr(y)/Ti(x)–Si catalysts, was investigated. It was found that 2.2 and 8 wt % are the optimum titanium and chromium contents in the synthesized catalysts for obtaining the highest catalytic activity. The superior catalytic performance of the Cr(8)/Ti(2.2)–Si catalyst can be attributed to a higher dispersion of the Cr species, as well as a higher content of the redox Cr species on the surface of the Cr/Ti–Si catalyst. The results showed that the Cr(8)/Ti(2.2)–Si catalyst efficiently dehydrogenated C_2H_6 in the presence of CO_2 giving a 52.3% ethane conversion and 48.0% ethylene yield at 700 °C reaction temperature.

Keywords: titania–silica; mesoporous nanocomposite; Cr catalyst; ethane oxidative dehydrogenation

1. Introduction

Ethylene is an essential feedstock used to produce a wide range of intermediate and final petrochemical products such as ethylene oxide, polyethylene, styrene, ethylene glycol, ethylbenzene and polyvinyl chloride [1–3]. Basically, thermal cracking of hydrocarbon cuts like natural gas and naphtha is the conventional process for ethylene production [4,5]. Energy consumption, rapid coke formation and enormous CO_2 emissions are the main drawbacks of the thermal cracking process [6–8].

However, catalytic ethane dehydrogenation using oxygen or carbon dioxide has been proposed as a good alternative to the thermal cracking process [9–12]. Nevertheless, the flammability of reactants mixture, exothermic nature of the reaction and over-oxidation of ethylene represent the obstacles of the dehydrogenation of ethane with oxygen [13–15].

On the other hand, the exploitation of CO_2 as a soft oxidant for ethane dehydrogenation overcomes these obstacles where the nature of reaction becomes endothermic and high ethane conversion with high ethylene yield and selectivity can be obtained at a low reaction temperature [11,12,15].

Over the last decades, a wide range of catalytic systems such as Cr [16–33], Ga [34–38], Ce [39,40], Zn [41], Co [2,42–44], La [45,46], Fe [47], V [48,49], Ni [44,46,50], Mo [44,51], In [52] and Mn [47,53] have been investigated for alkane dehydrogenation in the presence of CO_2. Among the studied materials, silica-supported chromium oxide has been proposed as the most promising catalytic system for ethane dehydrogenation [13,19,21,26,54].

It has been proven that the catalytic performance of the Cr/silica system mainly depends on the oxidation state of the Cr species, as well as the chromium–silica interaction. Cr species, with different oxidation states (Cr(III) and Cr(VI)), coexist on the surface of calcined Cr/silica catalytic systems, where Cr(VI) is the active phase or the component of the active phase for dehydrogenation or oxidative dehydrogenation reactions [23–25,55–57]. However, the concentration of reducible Cr(VI) on the surface of catalysts is crucial for the dehydrogenation reaction [58,59]. It has been reported that Cr(VI) will dominate when the Cr content is below the monolayer coverage over silica support. At the same time, when the Cr loading exceeds the monolayer coverage, the concentration Cr(III) increases, causing amorphous and crystalline Cr_2O_3 to form [25]. Therefore, the high catalytic performance of the Cr/silica system can be achieved when the Cr species are highly dispersed on the support and the Cr(VI)/Cr(III) ratio is high. On the other hand, high surface area mesoporous silica received more attention to be used as a support for high dispersion of chromium species. This material, in addition to its high surface area, which is 3–4 times higher than the commercial silica, has a uniform pore structure with narrow pore size distribution. So far, different mesoporous silica such as SBA-1 [24], SBA-15 [28], MSU-x [26,58] and MCM-41 [22,32,33] have been investigated in the dehydrogenation of ethane with CO_2 [24,26,27,29–33].

On the other hand, the interaction between Cr species and silica support is a key factor for the catalytic activity of this system. It has been found that modifying support surfaces with metal oxide enhances the dispersion of the active phases, as well as their interaction with the support [60–64]. Cecilia et al. doped SBA-15 silica with zirconium to generate a high number of acid centers that enhance the interaction of active phases, e.g., vanadium/phosphorous with Zr–SBA-15 for the glycerol dehydration reaction [60]. SBA-15 mesoporous silica was also modified with either titania or zirconia in order to improve the interaction of molybdenum as active phases for the hydro-desulfurization reaction [61]. Lizama et al. used titania modification to enhance the Ni–MO interaction with SBA-15 for the deep hydro-desulfurization reaction [62]. Furthermore, the Cr/TS-1 catalytic system was investigated for C_2H_6 dehydrogenation using CO_2; the catalyst exhibited reasonable activity [63].

In order to enhance the performance of the Cr species for ethane dehydrogenation, Ce oxide was employed to improve the interaction between Cr species and SBA-15 [28]. The results showed that the role of Ce was to help improve the dispersion of the Cr species over SBA-15. Bai et al. performed modification or the grafting of sulfate moieties into an SBA-15 support to boost the interaction of the support with the Cr species, which impacted catalytic activity [65] Recently, we modified mesoporous silica with titanium using the grafting method, then loading with chromium oxide. The prepared catalyst was tested for ethane dehydrogenation in the presence of CO_2 [64]. We found that modification of MCM41 by titanium promotes the surface properties of the synthesized catalyst by enhancing Cr–Ti–Si interactions, enhancing the activity in the ethane dehydrogenation [64].

Some of these grafting or modification processes were performed under an inert atmosphere in the presence of an organic solvent and repeating such process several times to increase the content of grafted elements. The process of grafting or modification usually takes place by forming mono or multiple layers on the surface of the support molecules. However, such modifications necessitated repeated, time-consuming and tedious processes. Composite materials that combine titania and silica in a mesoporous structure have attracted more attention due to their potential properties and applications in adsorption and catalysis.

In this context, it is predictable that the performance of the supported chromium oxide catalytic system can be enhanced if the mesoporous silica is replaced by titania–silica mesoporous nanocomposite and used as a catalyst support. In the present study, we report a simple, fast and facile route to prepare titania–silica mesoporous nanocomposites and use them as supports for chromium an oxide catalytic system. A series of Ti(x)–Si supports with Ti content in the range of 1.3–9.2 wt % were synthesized then impregnated with chromium precursor, characterized and tested in the oxidative dehydrogenation of C_2H_6 with CO_2. The ratio of titania/silica and the chromium content was optimized in this investigation.

2. Experimental

2.1. Materials

Tetraethoxysilane and tetraisopropyl orthotitanate as silica and titania precursors were purchased from Sigma-Aldrich. The chromium precursor (chromium nitrate nonahydrate) was purchased from Alfa Aesar. N-hexadecyltrimethylammonium chloride ($CH_3(CH_2)_{15}N(Cl)(CH_3)_3$, HTMACl, 25 wt % aqueous solution; surfactant) and ammonium hydroxide solution (NH_4OH, 28.0–30.0%) were received from Sigma-Aldrich.

2.2. Catalyst Preparation

MCM-41 support was prepared at room temperature using n-HTMACl and TEOS as a surfactant and silica precursor, respectively [27]. The titania–silica mesoporous nanocomposite was prepared at the same condition but with the presence of TTIP as the titania source. In this case, titania and silica sources were simultaneously added dropwise and a syringe pump was employed to control the hydrolysis rate of the precursors. The obtained powder was washed, dried and then calcined at 500 °C for 4 h. The same procedure was repeated but with different amounts of TTIP to obtain samples containing different TiO_2 contents.

In the next step, Cr(y)/Ti(x)–Si catalysts were formed by the incipient wetness impregnation method. The prepared samples were dried overnight before calcination in the air for 12 h at 650 °C. The final synthesized catalysts were represented as Cr(y)/Ti(x)–Si, where x and y denote the nominal weight percentage of Ti and Cr, respectively.

2.3. Catalyst Characterization

XRD patterns of the synthesized titania–silica mesoporous nanocomposite support, as well as supported chromium oxide catalysts, were conducted via a PANalyticalX'Pert PRO MPD (PANalytical, Netherlands) diffractometer. BET surface areas and pore size distributions of the prepared Ti(x)–Si and Cr(y)/Ti(x)–Si samples were measured by a Micromeritics Tristar II 3020 surface area and porosity analyzer (Micromeritics, Norcross, GA, USA). The ultraviolet–visible–diffuse reflectance (UV–Vis–DR) spectra were conducted using the Shimadzu UV-2100 spectrometer (Shimadzu, Kyoto, Japan). Elemental analysis was performed by PerkinElmer ICP optical emission spectrometers (Optima 8300 ICP-OES, Billerica, MA USA) and the contents of titanium and chromium were determined for all prepared samples. Temperature programmed reduction (H_2–TPR) analyses using a Micromeritics AutoChem II 2920 (Micromeritics, Norcross, GA, USA) instrument was employed to measure the reducibility of the synthesized catalysts. A Unicam 4000 FTIR spectrometer (Jasco, Easton, PA, USA) was used to characterize surface functional groups. A JEOL JEM-2100F transmission electron microscope (TEM) (JEOL, Tokyo, Japan) and JEOL JEM-7500F scanning electron microscope (SEM) (JEOL, Tokyo, Japan) were employed to investigate the sample's inner and outer morphologies, respectively, in addition to elemental dot mapping analysis.

2.4. Catalyst Evaluation

Ethane dehydrogenation with CO_2 was performed using the experimental rig shown in Figure S1. A 0.3 g amount of the catalyst was packed into a 6 mm reactor tube made of stainless steel. The reaction was carried out at atmospheric pressure and 600–700 °C reaction temperature. The reactants, $C_2H_6/CO_2/N_2$ (1/5/4), were introduced to the reactor system at a total flow rate of 45 mL/min. Pretreatment of the catalysts was conducted by introducing air at 600 °C for an hour before starting the reaction. The products of the dehydrogenation reaction and the unconverted reactants were measured using an online gas chromatograph (Agilent 6890 N, Agilent Santa Clara, CA, USA).

The percentage ethane conversion along with ethylene yield and selectivity were calculated based on the following equations:

$$C_2H_6 \text{ Conversion } (\%)\ (XC_2H_6) = \frac{n_{C_2H_{6in}} - n_{C_2H_{6out}}}{n_{C_2H_{6in}}} \times 100 \quad (1)$$

$$C_2H_4 \text{ Yield } (\%)\ (YC_2H_4) = \frac{n_{C_2H_4}}{n_{C_2H_{6in}}} \times 100 \quad (2)$$

$$C_2H_4 \text{ Selectivity } (\%)\ (SC_2H_4) = \frac{n_{C_2H_4}}{n_{C_2H_4} + n_{CH_4}} \times 100 \quad (3)$$

where n_i is a number of moles of the compound i.

3. Results and Discussion

3.1. Catalysts Characterization

TEM and EDX elemental analysis were conducted to have more insight into the internal structure and morphology of the synthesized Cr(8)/Ti(x)–Si catalysts, as well as the dispersity of chromium oxides on the support surface and the images, as presented in Figure 1. The TEM image of Cr(8)/MCM-41 samples shown in Figure 1A reveals the formation of large particle sizes of chromium oxides with a size range of 230–580 nm. The formation of large CrOx particles led to a lack of dispersity on the surface as shown in Figure 1A (green). On the other hand, the introduction of titania with 2.2 wt % led to a remarkable reduction of the catalyst particle size, as can be observed in the TEM images of Figure 1B, where the particle size of Cr_2O_3 reduced to less than 50 nm. The TEM images of the Cr(8)/Ti(9.2)–Si catalyst with higher titanium content shown in Figure 1C reveal the agglomeration of the chromium species on the catalyst; the average size was around 160 nm. On the other hand, the EDX images of the nanocomposite samples show improved dispersity of the Cr species, which can be referred to as their superior migration and interaction with titania, where the formation of Cr–O–Ti–O–Si linking bonding is thought to be the promotional role of titania in this catalytic system [64,66].

To identify the crystalline phases of the chromium-supported titania–silica mesoporous nanocomposite catalysts, X-ray diffraction peaks were measured and are presented in Figure 2. The peaks at 2θ = 24.5°, 33.6°, 36.2°, 41.5°, 50.2°, 54.9°, 63.4° and 65.18° could be indexed to the diffractions of (012), (104), (110), (113), (023), (116), (212) and (300) planes of the rhombohedral Cr_2O_3 crystals (JCPDS 00-006-0504). The diffraction peaks of Cr_2O_3 were observed in all prepared samples. In contrast, no diffraction peaks attributed to crystalline titania can be observed in the XRD patterns of Cr(8)/Ti(x)–Si catalysts due to the strong diffraction peaks of chromium and low crystallization tendency of TiO_2 at the examined titania content.

Figure 3A,B presents the N_2 adsorption–desorption isotherms and the distribution of pore sizes for all prepared Cr(8)/Ti(x)–Si catalysts. The textural properties of these samples were measured and the results are displayed in Table 1. The prepared samples possessed the isotherm of type IV along with a hysteresis loop of type H1 where both are the characteristics of mesoporous materials.

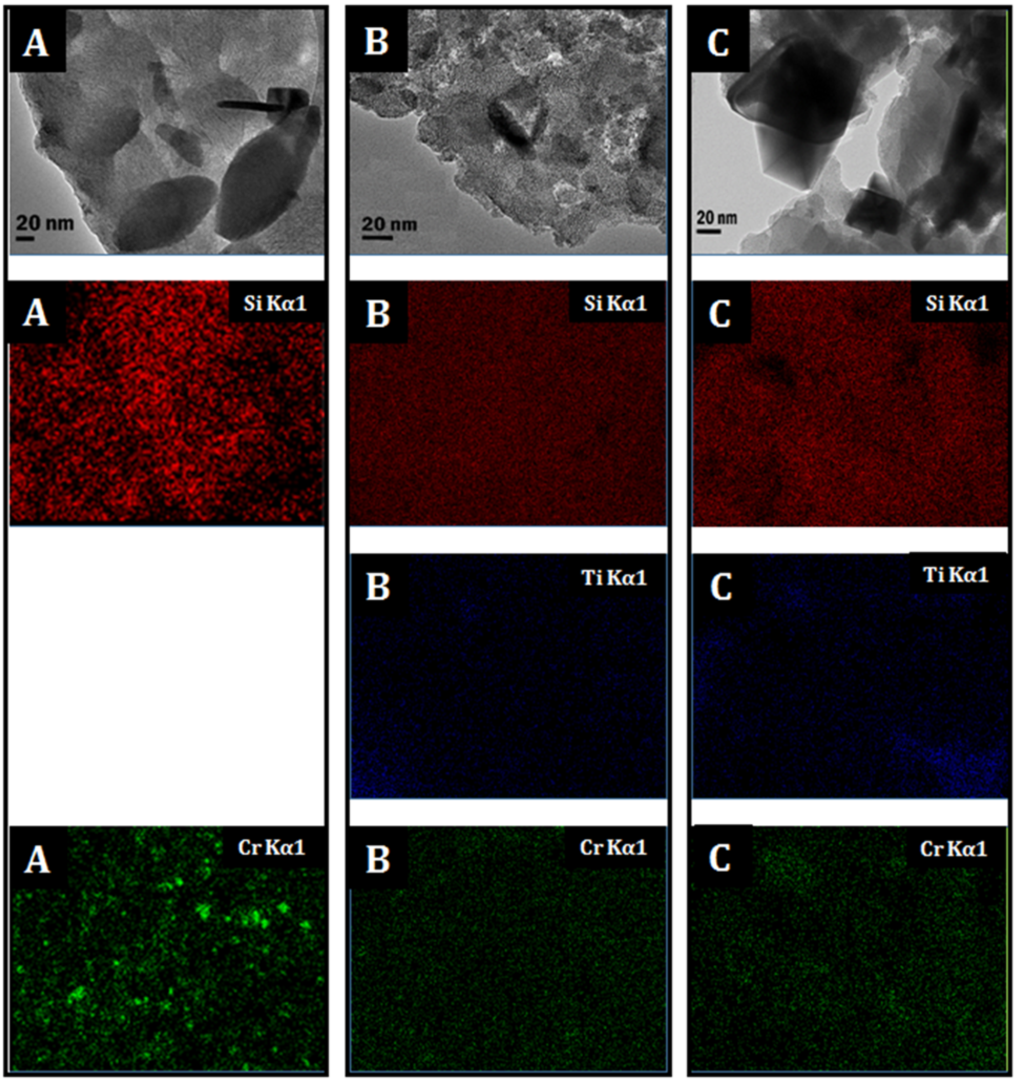

Figure 1. TEM images and EDX elemental mapping of (**A**) Cr(8)/MCM41, (**B**) Cr(8)/Ti(2.2)–Si and (**C**) Cr(8)/Ti(9.2)–Si catalysts.

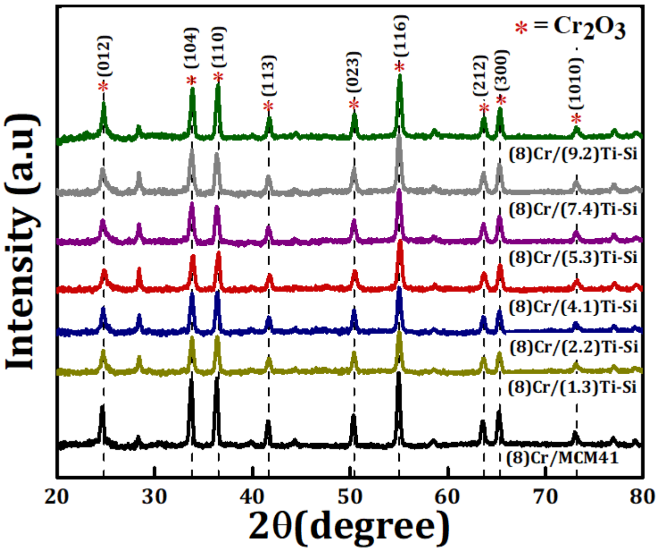

Figure 2. XRD patterns of Cr(8)/MCM-41 and Cr(8)/Ti(x)–Si prepared with varying titanium loadings, Ti wt %.

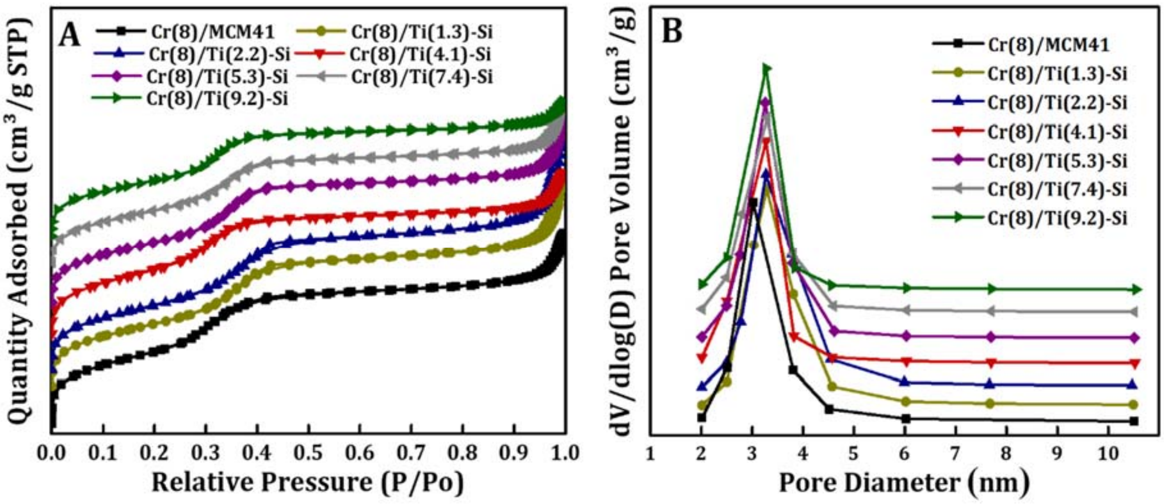

Figure 3. (**A**) N_2 isotherms and (**B**) pore size distribution of Cr(8)/MCM-41 and the Cr(8)/Ti(x)–Si catalysts prepared with varying titanium content, wt %.

Table 1. Textural properties of the MCM-41, Cr(8)/MCM-41, Ti(x)–Si nanocomposite and Cr(8)/Ti(x)–Si samples.

Catalyst	BET (m^2/g)	Pore Volume (cm^3/g)	Pore Size (nm)	Cr Surface Density (Cr/nm^2) [b]	Cr Particle Size [a] (nm)
Cr(8)/MCM-41	794	0.86	3.02	1.170	24.14
Cr(8)/Ti(1.3)–Si	750	0.98	3.29	1.235	20.03
Cr(8)/Ti(2.2)–Si	742	0.90	3.27	1.249	20.63
Cr(8)/Ti(4.1)–Si	730	0.87	3.27	1.269	20.61
Cr(8)/Ti(5.3)–Si	717	0.85	3.26	1.292	20.89
Cr(8)/Ti(7.4)–Si	643	0.75	3.29	1.441	21.35
Cr(8)/Ti(9.2)–Si	621	0.63	3.28	1.491	21.82

[a] Estimated by Scherer's equation from XRD patterns at $2\theta \approx 55$. [b] Dispersity of Chromium (Cr Surface Density = NA × (Cr wt %/Cr mol.wt)/SBET) [33,64,67].

Capillary condensation of nitrogen molecules within the pores of MCM-41 and Ti(x)–Si samples occurred when the relative pressure exceeded 0.3, suggesting the mesoporous nature of the synthesized nanocomposite. Figure 3B shows the distribution of the pore size calculated using the BJH method. Cr(8)/MCM-41 and Cr(8)/Ti(x)–Si mesoporous nanocomposite catalysts display a uniform and narrow pore size distribution centered at 3 nm for the former and around 3.3 nm for the nanocomposite (Table 1). Moreover, the synthesized nanocomposite samples show high BET surface areas that tend to decrease with increasing TiO_2 content (Table 1).

The chemical composition, as well as the oxidation states of the elements, was investigated for all prepared samples by using X-ray photoelectron spectroscopy (XPS). The XPS measurement was conducted for Cr(8)/MCM-41 and Cr(8)/Ti(x)–Si (x = 2.2, 5.3 and 9.2 wt %) samples. The spectra are presented in Figure S2 and Figure 4. The XPS survey spectra of these samples show that chromium, oxygen, silicon and carbon elements are present in all prepared samples (Figure S2A). The peak positions of all elements are in agreement with the values reported in the literature [68]. Moreover, an additional peak centered at 456.9 eV can be observed in the XPS survey spectra of titania–silica mesoporous nanocomposite samples which can be due to Ti2p binding energy.

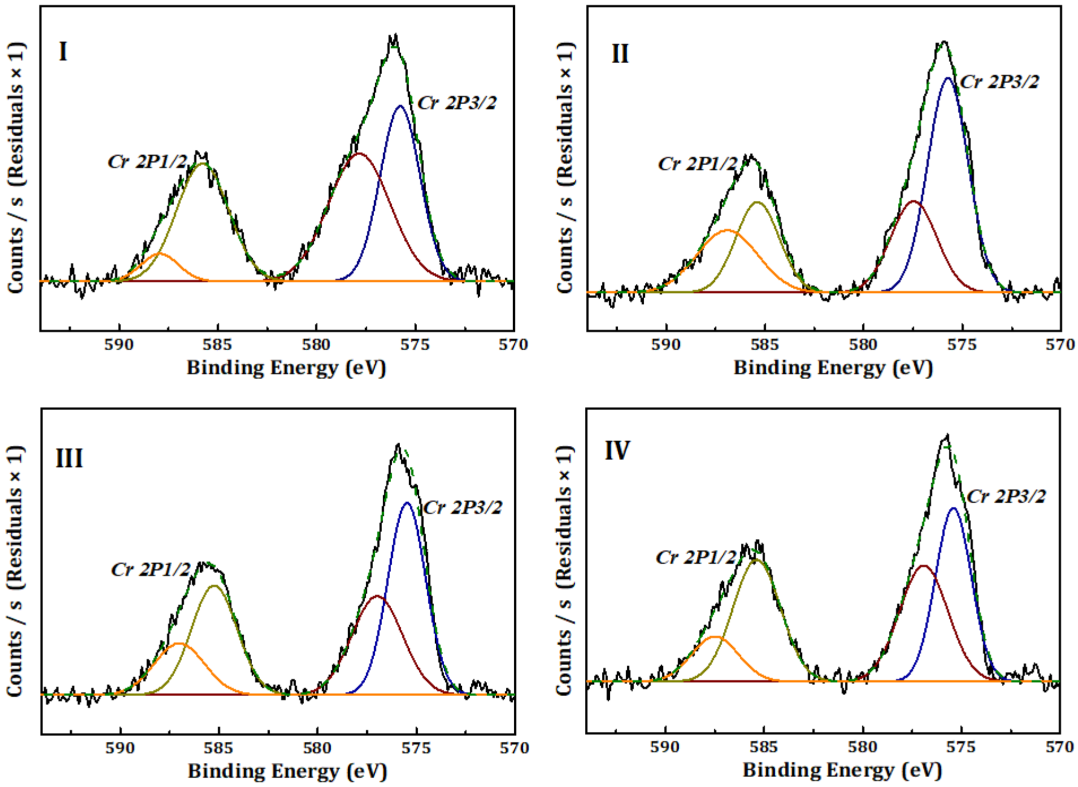

Figure 4. Cr2p XPS spectrum of Cr(8)/MCM-41 (**I**) and Cr(8)/Ti(x)–Si composite prepared with varying titanium loading, where x = 2.2(**II**), 5.3(**III**) and 9.2(**IV**) wt %.

To better understand the composition and crystalline phase of TiO_2, the high-resolution XPS spectra of Ti2p of Cr(8)/(x)–Ti–Si samples were measured. Figure S2B shows that the Ti2p spectrum can be deconvoluted into two main peaks. The peak located at 464 eV corresponds to Ti ($2p_{1/2}$) while the peak at 458.3 eV is assigned to Ti ($2p_{3/2}$). The difference between the Ti ($2p_{1/2}$) and Ti ($2p_{3/2}$) core level is around 5.7 eV, which indicates the presence of a normal state of Ti^{4+} in the anatase phase of TiO_2 [69,70].

The finely scanned XPS spectra of Cr2p of all synthesized samples are shown in Figure 4. The spectra are composed of two peaks with binding energies of 575.60 and 585 eV that can be attributed to the $Cr2p_{3/2}$ and $Cr2p_{1/2}$ levels, respectively. By using peak-fitting software, these XPS peaks can be further divided into two more peaks representing Cr(VI) and Cr(III) ions. The $Cr2p_{3/2}$ spectrum consists of peaks at 575.5(+/−0.5) and 577.68 which can be assigned to Cr(III) and Cr(VI) ions, respectively. The quantitative results are presented in Table 2.

Table 2. XPS results of Cr(8)/MCM-41 and Cr(8)/Ti(x)–Si-nanocomposites where x = 2.2, 5.3 and 9.2 wt % catalysts.

Catalyst	Cr $2p_{3/2}$ Binding Energy (eV)		Cr(VI)/Cr(III)
	Cr(VI)	Cr(III)	
Cr(8)/MCM-41	575.77	577.84	0.882
Cr(8)/Ti(2.2)–Si	575.74	577.47	2.062
Cr(8)/Ti(5.3)–Si	575.49	576.98	1.451
Cr(8)/Ti(9.2)–Si	575.41	576.92	1.052

It can be observed that all synthesized catalysts have almost similar binding energy (BE) values, but with variances in the Cr(VI)/Cr(III) ratios. The Cr(VI)/Cr(III) ratio of the Cr(8)/Ti-(X)–Si sample (x = 2.2, 5.3 and 9.2 wt %) significantly decreases with increasing TiO_2 contents in the mesoporous composite, while the Cr(8)/Ti(2.2)–Si showed the highest Cr(VI)/Cr(III) ratio of 2.062. Based on the domination of Cr(VI) as the active phase of chromium species, it is expected that the Cr(8)/Ti(2.2)–Si catalyst will show high catalytic performance toward ethane dehydrogenation.

More information about the oxidation state of chromium oxide was reached from analysis using ultraviolet–visible–diffuse reflectance (UV–Vis–DR) and the spectra are shown in Figure 5. The absorbance of Cr(8)/Ti(x)–Si samples were higher than the Cr(8)/MCM-41 sample due to the existence of titania, which can be considered spots for absorbing photons for the prepared nanocomposite catalysts. Beside the reported data, the absorption bands at 260 and 370 nm can be attributed to the $O^{2-} \rightarrow Cr(VI)$ charge transfer transition of the tetrahedral chromate species. Nevertheless, the bands at 470 and 600 nm can be assigned to the d–d transitions of octahedral Cr(III) species in Cr_2O_3 or CrO_x clusters [16,59,71–74].

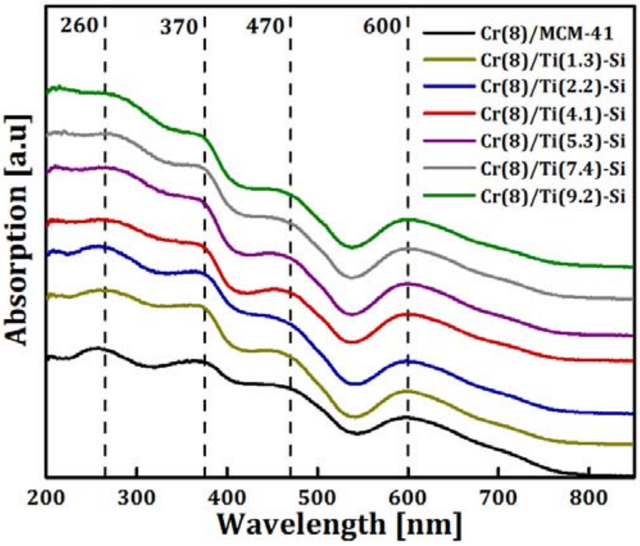

Figure 5. UV–Vis–DR spectra of Cr(8)/MCM-41 and Cr(8)/T(x)–Si catalysts prepared with varying titanium content wt %.

The reducibility of the supported chromium oxide on both pure mesoporous silica and titania–silica mesoporous nanocomposites has been investigated using H_2–TPR measurements and the profiles are presented in Figure 6 and Table 3. One can observe that two obvious peaks occurred in the H_2–TPR profiles spectrum for all samples, which can be assigned to Cr(VI) species reduction. From the literature, the peak around 270 °C was attributed to the reduction of formed Cr(VI) species on the catalyst surface, while the reduction peak at 405–430 °C was attributed to the reduction of the interacted Cr(VI) species with the support framework [19,27,75]. These results are in agreement with XPS and the UV–Vis–DRS results that proved clearly the coexistence of both Cr(VI) and Cr(III) species on the catalyst surface. It is noteworthy that the TPR profile of Cr(8)/MCM-41 shows a sharp reduction peak around 270 °C, and a broad small peak around 430 °C. This suggests that most Cr(VI) species are existing as bulk oxides that disperse outside the silica matrix. In contrast, a small fraction of chromate species binds with the MCM-41 framework, so that a weak interaction between chromium species and silica support was formed [27]. On the other hand, H_2–TPR profiles for Cr(8)/Ti(x)–Si nanocomposites show different intensities of reduction peak compared with those of MCM-41. Based on the results, the intensity of the 270 °C reduction peak is lowered when the titania–silica nanocomposite was employed as a support instead of silica, indicating that most Cr(VI) species interacted well with the nanocomposite support, and less reducible Cr species present apart from the support. Simultaneously, increased intensity of the second reduction peak (at around 405 °C) suggests that the Cr(8)/Ti(2.2)–Si sample possesses excellent chromium-support interaction.

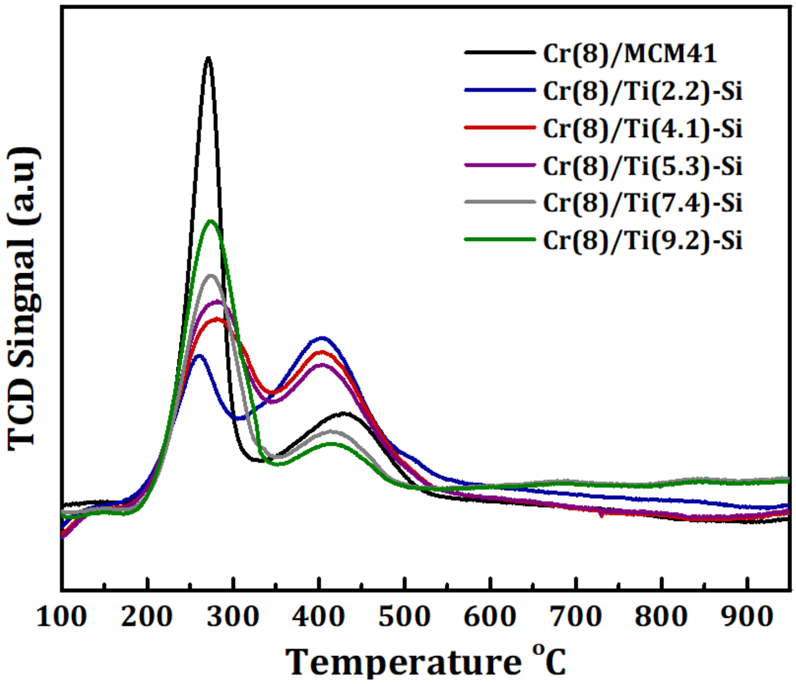

Figure 6. H_2–TPR profiles spectra of Cr(8)/MCM-41 and Cr(8)/Ti(x)–Si-nanocomposite catalysts prepared with varying titanium content wt %.

Table 3. Reducibility data obtained from H_2–TPR profiles of Cr(8)/MCM-41 and Cr(8)/Ti(x)–Si catalysts.

Catalysts	**H_2 Uptake (µmol/g)**	**H_2/Cr Total (mol/mol)**	**First Cr(VI) Peak Area**	**Second Cr(VI) Peak Area**	**Second Cr(VI) Peak Area/Total Area**
Cr(8)/MCM-41	386.14	0.251	2.06	1.13	0.35
Cr(8)/Ti(2.2)–Si	384.16	0.249	0.86	2.52	0.75
Cr(8)/Ti(4.1)–Si	368.63	0.240	1.63	2.29	0.58
Cr(8)/Ti(5.3)–Si	359.13	0.233	1.73	2.12	0.55
Cr(8)/Ti(7.4)–Si	342.48	0.223	1.60	0.73	0.31
Cr(8)/Ti(9.2)–Si	327.26	0.213	2.11	0.66	0.24

On the other hand, the intensity of the first peak slightly increased with increasing TiO_2 content from 2.2 to 9.2 wt % in the nanocomposite samples. This peak is assigned to the reduction of both Cr(VI) and Ti^{4+} that interacted with the framework of silica [76,77]. The peak intensity varies due to the rise of Ti^{4+} content which is also reduced at this temperature. In contrast, raising titania content above 2.2 wt % decreases the intensity of the 405–430 °C peak, at which Cr(VI) is in the interaction with silica support undergoes reduction. This interaction can be explained by the formation of a thicker titania layer which isolates the reducible Cr species from the silica matrix [64].

Hydrogen uptake per each gram of catalyst, hydrogen/chromium ratio (mol/mol ratio) and Cr(VI) reduction peaks area are illustrated in Table 3. From these results, the highest values of H_2 uptake and H_2/Cr ratio were recorded for the Cr(8)/MCM-41 and Cr(8)/Ti(2.2)–Si catalysts. The H_2 consumption for these two samples is almost the same owing to their similar chromium content. It is interesting to note that Cr(VI) distribution between the surface and inside the matrix of these two samples are totally different. Table 3 shows that 75% of Cr(VI) species are in robust interaction with the support framework for Cr(8)/Ti(2.2)–Si sample compared to only 35% for Cr(8)/MCM-41 one. Hence, the high stability of reducible chromium for Cr(8)/Ti(2.2)–Si catalyst is expected.

Furthermore, increasing titania content above 2.2% led to a steep decrease of the interacted fraction of reducible chromium with the silica matrix in the nanocomposite catalyst, reaching 0.24 for the Cr(8)/Ti(9.2)–Si catalyst. This result suggests that a continuous increase of titania contents within the mesoporous nanocomposite could cause insulation of the Cr species from the silica matrix. Moreover, H_2 consumption per each gram of the catalyst and H_2/Cr ratio shows the same tendency, where the H_2 uptake fell from 384.16 μmol H_2/g for Cr(8)/Ti(2.2)–Si to 327.26 μmol H_2/g for Cr(8)/Ti(9.2)–Si while H_2/Cr ratio dropped from 0.249 to 0.213 mol/mol for the same catalysts. It can be concluded that the fraction of Cr(III) species increases with increasing titania percent in the nanocomposite, where Cr_2O_3 the phase dominates at the higher titania content samples. These findings are well consistent with the information obtained from XRD, XPS and UV–Vis–DR measurements.

By merging TPR results with XPS, UV–Vis–DR and XRD data, it can be noted that the Cr(8)/Ti(2.2)–Si catalyst has a high concentration of reducible chromium species with uniform dispersion and strong interaction with the mesoporous support structure. Therefore, high catalytic activity with good stability is expected for this catalytic system. In contrast, increasing titania percent above 2.2 wt % increased the concentration of non-redox Cr species that, in turn, could drop the catalytic activity.

3.2. Catalytic Activity

The catalytic activity of the synthesized catalysts was examined for the ethane dehydrogenation in the presence of CO_2 as oxidant and results are displayed in Figure 7A–C). The catalytic activities of all synthesized catalysts are clearly dependent on the reaction temperature.

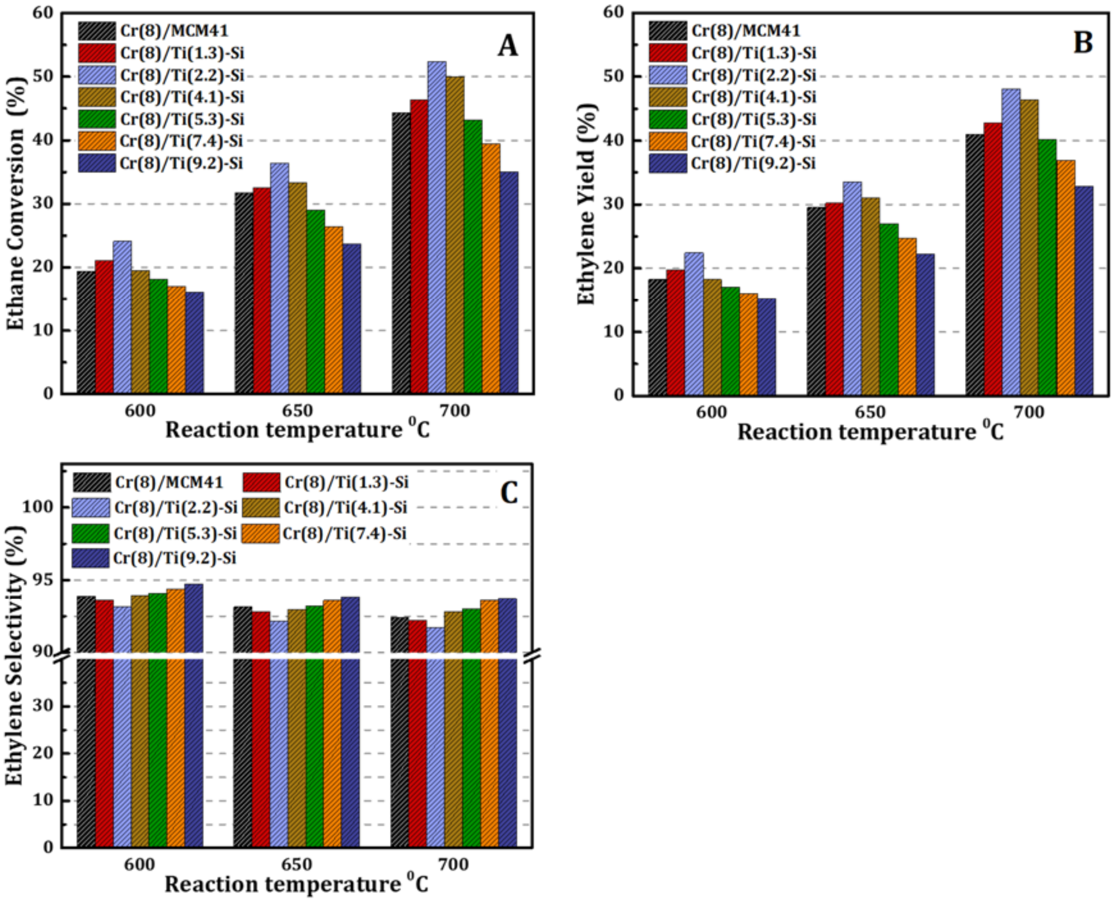

Figure 7. Effect of Ti loading on (**A**) ethane conversions and (**B**) ethylene selectivity and (**C**) ethylene yield of Cr(8)/Ti(x)–Si nanocomposite catalysts at different reaction temperatures.

Ethane conversion, as well as ethylene yield, increases with elevating reaction temperature owing to the endothermic nature of this reaction while the ethylene selectivity slightly drops due to cracking side reactions that dominate at high reaction temperatures. From Figure 7, the maximum ethane conversion over the Cr(8)/MCM-41 catalyst was 44.4% with an ethylene yield of 41.0%. Using the titania–silica mesoporous nanocomposite leads to a significant improvement in the performance, where both ethane conversion and ethylene yield rise steeply with increasing titania contents up to 2.2 wt %. The highest values of conversion and yield were 52.3% and 48.0%, respectively, at 700 °C. A further increase in the titania content led to a drop in both ethane conversion and ethylene yield due to the formation of less or non-active Cr species. The recorded ethylene selectivity over all tested catalysts was more than 90%, which agrees with the literature over similar catalytic system (Cr/silica) [14,15,22,63,64,67]. Hence, the Cr(8)/Ti(2.2)–Si catalyst is superior among other catalysts at all reaction temperatures. The high catalytic conversion of Cr(8)/Ti(2.2)–Si catalyst Cr(8)/Ti(2.2)–Si catalyst can be explained based on the chemical and physical properties of the developed sample. The chemical properties revealed by TPR and XPS analyses have indicated that active chromium ratio Cr^{+6}/Cr^{+3} was highest in the Cr(8)/Ti(2.2)–Si catalyst. In addition, this sample also showed a superior percentage of reducible Cr^{6+} species that are responsible for effective ethane dehydrogenation. On the other hand, physical properties obtained by microscopy that included TEM imaging and elemental mapping showed the two main points of small sizes of the Cr species along with their better dispersity. Moreover, based on the findings of Jehng et al. [66], TiO_2 at low a concentration (2.2 wt %) will provide a promotional impact by constructing linking bonding (Cr–O–Ti–O–Si) between silica and Cr species through Ti ones.

On the other hand, the influence of the Cr contents on the catalytic activity was also studied and the results are presented in Figure 8. Both ethane conversion and ethylene yield increased by increasing the chromium loading and both reached their maximum values for 8 wt % of the Cr catalyst. A further increase of Cr loading decreased both values because of the formation of a non-redox Cr species. Crystalline α-Cr_2O_3 was found to be less active in the dehydrogenation reactions [22,27].

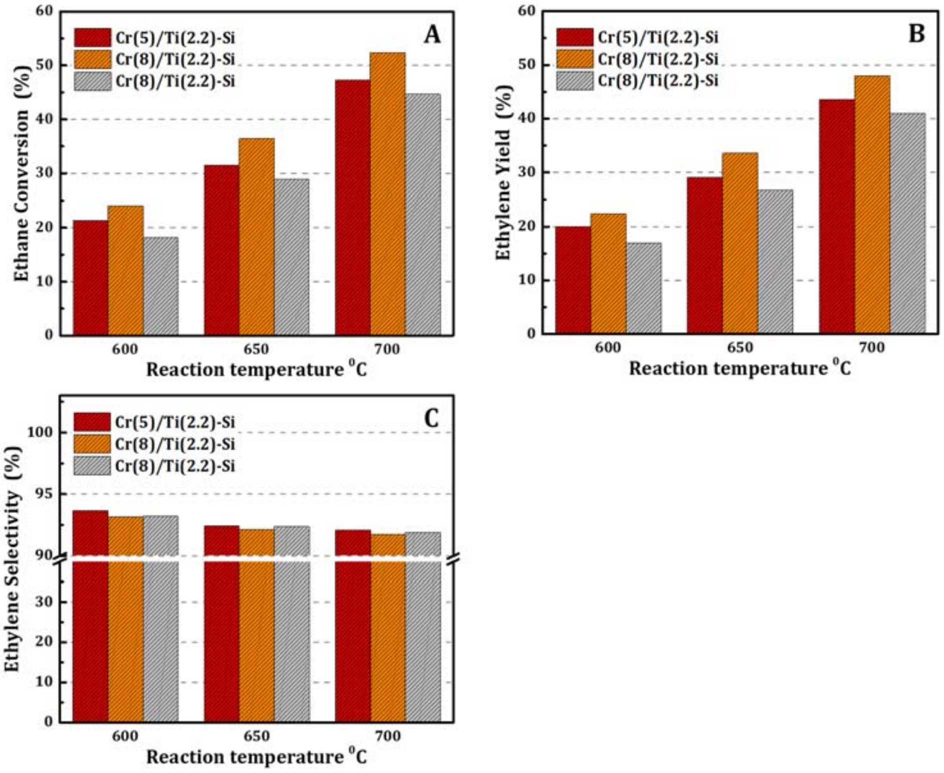

Figure 8. Effect of Cr loading on (**A**) ethane conversions, (**B**) ethylene yield (**C**) and selectivity of Cr(y)/Ti(2.2)–Si nanocomposite catalysts at various reaction temperatures.

Catalytic stability of the superior catalyst, Cr(8)/Ti(2.2)–Si, was also investigated by continuously running the dehydrogenation reaction over this catalyst for 10 h. The results are displayed in Figure 9. It can be seen that ethane conversion and ethylene yield over the Cr(8)/Ti(2.2)–Si catalyst decreases slowly with time-on-stream while the selectivity to ethylene almost remains constant around 92–95% after 10 h of reaction time. Lowering the number of reducible chromium species in addition to coke formation are reasonable explanations for such a reduction in catalytic activity. However, Cr(8)/Ti(2.2)–Si catalyst still exhibited reasonable stability after 10 h on stream operation. Therefore, as conclusive remarks, the concentration of high oxidation state reducible chromium species (Cr(VI)) with small size and uniform dispersion are responsible for the superior catalytic performance of the Cr(8)/Ti(2.2)–Si catalyst.

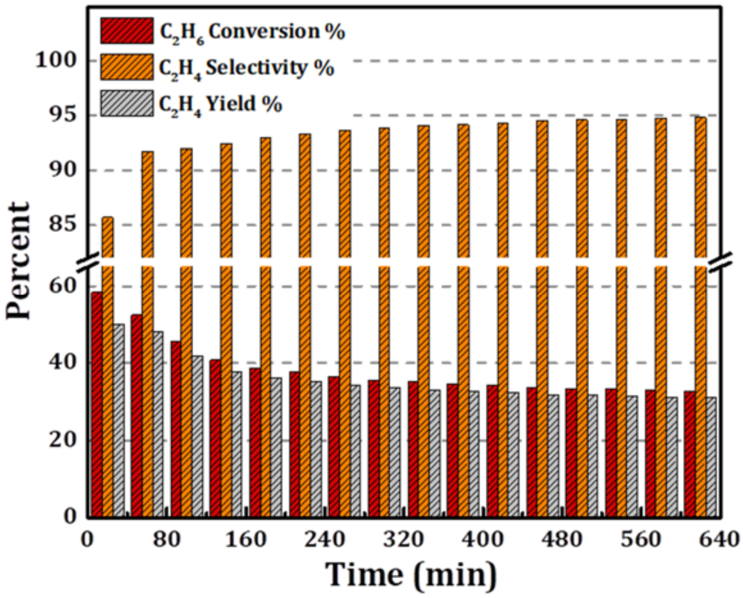

Figure 9. Ethane conversion, ethylene yield and selectivity versus time-on-stream over Cr(8)/Ti(2.2)–Si Nanocomposite catalyst at 700 °C.

4. Conclusions

In this study, titania–silica mesoporous nanocomposites were synthesized with different titanium contents before impregnation of chromium oxide and examination for oxidative ethane dehydrogenation using CO_2. The variation of the titanium content changed the relative crystallinity, as well as the surface area of Ti(x)–Si samples. The characterization results indicated that Ti(x)–Si, with a Ti content of 2.2%, has superior relative crystallinity with appropriate surface area and uniformity, as well as a greater ratio of Cr(VI)/Cr(III). The presence of 2.2% titanium stabilized the reducible Cr species at their high oxidation number in addition to the enhancement of chromium dispersity and metal–support interaction. It has also been found that for superior catalytic activity, the optimum chromium content is 8 wt %. The highest ethane conversions and ethylene yields obtained at 700 °C over the Cr(8)/Ti(2.2)–Si catalyst were 52.3% and 48.0%. Furthermore, this nanocomposite catalyst has shown good stability for more than 10 h on the stream.

Supplementary Materials: The following are available online at http://www.mdpi.com/2073-4352/10/4/322/s1, Figure S1: Experimental setup for the oxidative dehydrogenation (ODH) of C_2H_6 with CO_2. Figure S2: (A) XPS survey spectra of Cr(8)/MCM-41(I) and Cr(8)/Ti(x)-Si-Composite and (B) Ti2p XPS spectrum of Cr(8)/Ti(x)-Si-Composite prepared with varying titanium loading, where x (a) 0.0 (b)2.2, (c) 5.3, and (d) 9.2 Ti wt %. Table S1: Comparison of catalytic performance of various catalysts for ethane dehydrogenation with CO_2.

Author Contributions: Conceptualization, writing-review editing: A.E.A. and S.M.A.-Z. Investigation, writing-original draft, writing-review editing: A.S.A.-A., A.M.E.-T., and A.E.A. Methodology and formal analysis: A.S.A.-A., A.K., and A.M.E.-T. All authors have read and agreed to the published version of the manuscript.

Funding: This work was funded by Researchers Supporting Project number (RSP-2019/90), King Saud University, Riyadh, Saudi Arabia.

Conflicts of Interest: The authors declare no conflict of interest.

References

1. Gärtner, C.A.; van Veen, A.C.; Lercher, J.A. Oxidative Dehydrogenation of Ethane: Common Principles and Mechanistic Aspects. *ChemCatChem* **2013**, *5*, 3196–3217. [CrossRef]
2. Koirala, R.; Buechel, R.; Pratsinis, S.E.; Baiker, A. Silica is preferred over various single and mixed oxides as support for CO_2-assisted cobalt-catalyzed oxidative dehydrogenation of ethane. *Appl. Catal. A* **2016**, *527*, 96–108. [CrossRef]
3. Bhasin, M.M.; McCain, J.H.; Vora, B.V.; Imai, T.; Pujadó, P.R. Dehydrogenation and oxydehydrogenation of paraffins to olefins. *Appl. Catal. A* **2001**, *221*, 397–419. [CrossRef]
4. Ren, T.; Patel, M.; Blok, K. Olefins from conventional and heavy feedstocks: Energy use in steam cracking and alternative processes. *Energy* **2006**, *31*, 425–451. [CrossRef]
5. Zimmermann, R.W.H. Ethylene. In *Ullmann's Encyclopedia of Industrial Chemistry*; Wiley: Weinheim, Germany, 2009; Volume 13, pp. 465–529.
6. Dharia, D.; Letzsch, W.; Kim, H.; McCue, D.; Chapin, L. Increase light olefins production: New methods based on proven FCC technology provide additional olefins source. *Hydrocarb. Process* **2004**, *83*, 61–66.
7. Grace Chan, K.; Inal, F.; Senkan, S. Suppression of coke formation in the steam cracking of alkanes: Ethane and propane. *Ind. Eng. Chem. Res.* **1998**, *37*, 901–907. [CrossRef]
8. Resasco, D.E.; Haller, G.L. Catalytic dehydrogenation of lower alkanes. In *Catalysis*; Spivey, J.J., Agarwal, S.K., Eds.; The Royal Society of Chemistry: London, UK, 1994; Volume 11, pp. 379–411.
9. Bañares, M.A. Supported metal oxide and other catalysts for ethane conversion: A review. *Catal. Today* **1999**, *51*, 319–348. [CrossRef]
10. Cavani, F.; Trifirò, F. The oxidative dehydrogenation of ethane and propane as an alternative way for the production of light olefins. *Catal. Today* **1995**, *24*, 307–313. [CrossRef]
11. Wang, S.; Zhu, Z.H. Catalytic Conversion of Alkanes to Olefins by Carbon Dioxide Oxidative Dehydrogenation: A Review. *Energy Fuel* **2004**, *18*, 1126–1139. [CrossRef]
12. Mimura, N.; Okamoto, M.; Yamashita, H.; Oyama, S.T.; Murata, K. Oxidative Dehydrogenation of Ethane over Cr/ZSM-5 Catalysts Using CO_2 as an Oxidant. *J. Phys. Chem. B* **2006**, *110*, 21764–21770. [CrossRef]
13. Wang, S.; Murata, K.; Hayakawa, T.; Hamakawa, S.; Suzuki, K. Dehydrogenation of ethane with carbon dioxide over supported chromium oxide catalysts. *Appl. Catal. A* **2000**, *196*, 1–8. [CrossRef]
14. Li, Y.; He, X.; Wu, S.; Zhang, K.; Zhou, G.; Liu, J.; Zhen, K.; Wu, T.; Cheng, T. Cr-MCM-41 molecular sieves crystallized at room temperature for reaction of ethane with CO_2. *J. Nat. Gas Chem.* **2005**, *14*, 207–212.
15. Al-Awadi, A.S.; El-Toni, A.M.; Alhoshan, M.; Khan, A.; Shar, M.A.; Abasaeed, A.E.; Al-Zahrani, S.M. Synergetic Impact of Secondary Metal Oxides of Cr-M/MCM41 Catalyst Nanoparticles for Ethane Oxidative Dehydrogenation Using Carbon Dioxide. *Crystals* **2019**, *10*, 7. [CrossRef]
16. Cheng, Y.; Zhang, F.; Zhang, Y.; Miao, C.; Hua, W.; Yue, Y.; Gao, Z. Oxidative dehydrogenation of ethane with CO_2 over Cr supported on submicron ZSM-5 zeolite. *Chin. J. Catal.* **2015**, *36*, 1242–1248. [CrossRef]
17. Rahmani, F.; Haghighi, M.; Amini, M. The beneficial utilization of natural zeolite in preparation of Cr/clinoptilolite nanocatalyst used in CO_2-oxidative dehydrogenation of ethane to ethylene. *J. Ind. Eng. Chem.* **2015**, *31*, 142–155. [CrossRef]
18. Rahmani, F.; Haghighi, M.; Mahboob, S. CO_2-enhanced dehydrogenation of ethane over sonochemically synthesized Cr/clinoptilolite-ZrO_2 nanocatalyst: Effects of ultrasound irradiation and ZrO_2 loading on catalytic activity and stability. *Ultrason. Sonochem.* **2016**, *33*, 150–163. [CrossRef] [PubMed]
19. Michorczyk, P.; Pietrzyk, P.; Ogonowski, J. Preparation and characterization of SBA-1–supported chromium oxide catalysts for CO_2 assisted dehydrogenation of propane. *Microporous Mesoporous Mater.* **2012**, *161*, 56–65. [CrossRef]
20. Ramesh, Y.; Thirumala Bai, P.; Hari Babu, B.; Lingaiah, N.; Rama Rao, K.S.; Prasad, P.S.S. Oxidative dehydrogenation of ethane to ethylene on Cr_2O_3/Al_2O_3–ZrO_2 catalysts: The influence of oxidizing agent on ethylene selectivity. *Appl. Petrochem. Res.* **2014**, *4*, 247–252. [CrossRef]
21. Deng, S.; Li, H.; Li, S.; Zhang, Y. Activity and characterization of modified Cr_2O_3/ZrO_2 nano-composite catalysts for oxidative dehydrogenation of ethane to ethylene with CO_2. *J. Mol. Catal. A Chem.* **2007**, *268*, 169–175. [CrossRef]

22. Asghari, E.; Haghighi, M.; Rahmani, F. CO_2 Oxidative Dehydrogenation of Ethane to Ethylene over Cr/MCM-41 Nanocatalyst Synthesized via Hydrothermal/Impregnation Methods: Influence of Chromium Content on Catalytic Properties and Performance. *J. Mol. Catal. A Chem.* **2016**, *418*, 115–124. [CrossRef]
23. Botavina, M.A.; Martra, G.; Agafonov, Y.A.; Gaidai, N.A.; Nekrasov, N.V.; Trushin, D.V.; Coluccia, S.; Lapidus, A.L. Oxidative dehydrogenation of C3–C4 paraffins in the presence of CO_2 over $CrOx/SiO_2$ catalysts. *Appl. Catal. A* **2008**, *347*, 126–132. [CrossRef]
24. Michorczyk, P.; Ogonowski, J.; Niemczyk, M. Investigation of catalytic activity of CrSBA-1 materials obtained by direct method in the dehydrogenation of propane with CO_2. *Appl. Catal. A* **2010**, *374*, 142–149. [CrossRef]
25. Jóźwiak, W.K.; Ignaczak, W.; Dominiak, D.; Maniecki, T.P. Thermal stability of bulk and silica supported chromium trioxide. *Appl. Catal. A* **2004**, *258*, 33–45. [CrossRef]
26. Liu, L.; Li, H.; Zhang, Y. Mesoporous silica-supported chromium catalyst: Characterization and excellent performance in dehydrogenation of propane to propylene with carbon dioxide. *Catal. Commun.* **2007**, *8*, 565–570. [CrossRef]
27. Michorczyk, P.; Ogonowski, J.; Kuśtrowski, P.; Chmielarz, L. Chromium oxide supported on MCM-41 as a highly active and selective catalyst for dehydrogenation of propane with CO_2. *Appl. Catal. A* **2008**, *349*, 62–69. [CrossRef]
28. Shi, X.; Ji, S.; Wang, K. Oxidative Dehydrogenation of Ethane to Ethylene with Carbon dioxide over Cr–Ce/SBA-15 Catalysts. *Catal. Lett.* **2008**, *125*, 331–339. [CrossRef]
29. Zhang, X.; Yue, Y.; Gao, Z. Chromium Oxide Supported on Mesoporous SBA-15 as Propane Dehydrogenation and Oxidative Dehydrogenation Catalysts. *Catal. Lett.* **2002**, *83*, 19–25. [CrossRef]
30. Wang, Y.; Ohishi, Y.; Shishido, T.; Zhang, Q.; Yang, W.; Guo, Q.; Wan, H.; Takehira, K. Characterizations and catalytic properties of Cr-MCM-41 prepared by direct hydrothermal synthesis and template-ion exchange. *J. Catal.* **2003**, *220*, 347–357. [CrossRef]
31. Wang, Y.; Ohishi, Y.; Shishido, T.; Zhang, Q.; Takehira, K. Cr-MCM-41 for selective dehydrogenation of lower alkanes with carbon dioxide. In *Studies in Surface Science and Catalysis*; Park, S.-E., Ryoo, R., Ahn, W.-S., Lee, C.W., Chang, J.-S., Eds.; Elsevier: Amsterdam, The Netherlands, 2003; Volume 146, pp. 725–728.
32. Takehira, K.; Ohishi, Y.; Shishido, T.; Kawabata, T.; Takaki, K.; Zhang, Q.; Wang, Y. Behavior of active sites on Cr-MCM-41 catalysts during the dehydrogenation of propane with CO_2. *J. Catal.* **2004**, *224*, 404–416. [CrossRef]
33. Al-Awadi, A.S.; El-Toni, A.M.; Alhoshan, M.; Khan, A.; Labis, J.P.; Al-Fatesh, A.; Abasaeed, A.E.; Al-Zahrani, S.M. Impact of precursor sequence of addition for one-pot synthesis of Cr-MCM-41 catalyst nanoparticles to enhance ethane oxidative dehydrogenation with carbon dioxide. *Ceram. Int.* **2019**, *45*, 1125–1134. [CrossRef]
34. Nakagawa, K.; Kajita, C.; Ide, Y.; Okamura, M.; Kato, S.; Kasuya, H.; Ikenaga, N.O.; Kobayashi, T.; Suzuki, T. Promoting effect of carbon dioxide on the dehydrogenation and aromatization of ethane over gallium-loaded catalysts. *Catal. Lett.* **2000**, *64*, 215–221. [CrossRef]
35. Nakagawa, K.; Kajita, C.; Okumura, K.; Ikenaga, N.-O.; Nishitani-Gamo, M.; Ando, T.; Kobayashi, T.; Suzuki, T. Role of Carbon Dioxide in the Dehydrogenation of Ethane over Gallium-Loaded Catalysts. *J. Catal.* **2001**, *203*, 87–93. [CrossRef]
36. Shen, Z.; Liu, J.; Xu, H.; Yue, Y.; Hua, W.; Shen, W. Dehydrogenation of ethane to ethylene over a highly efficient Ga_2O_3/HZSM-5 catalyst in the presence of CO_2. *Appl. Catal. A* **2009**, *356*, 148–153. [CrossRef]
37. Koirala, R.; Buechel, R.; Krumeich, F.; Pratsinis, S.E.; Baiker, A. Oxidative Dehydrogenation of Ethane with CO_2 over Flame-Made Ga-Loaded TiO_2. *ACS Catal.* **2015**, *5*, 690–702. [CrossRef]
38. Michorczyk, P.; Ogonowski, J. Dehydrogenation of propane to propene over gallium oxide in the presence of CO_2. *Appl. Catal. A* **2003**, *251*, 425–433. [CrossRef]
39. Valenzuela, R.X.; Bueno, G.; Cortés Corberán, V.; Xu, Y.; Chen, C. Selective oxidehydrogenation of ethane with CO_2 over CeO_2-based catalysts. *Catal. Today* **2000**, *61*, 43–48. [CrossRef]
40. Valenzuela, R.X.; Bueno, G.; Solbes, A.; Sapiña, F.; Martínez, E.; Cortés Corberán, V. Nanostructured ceria-based catalysts for oxydehydrogenation of ethane with CO_2. *Top. Catal.* **2001**, *15*, 181–188. [CrossRef]
41. Li, H.; Yue, Y.; Miao, C.; Xie, Z.; Hua, W.; Gao, Z. Dehydrogenation of ethylbenzene and propane over Ga_2O_3–ZrO_2 catalysts in the presence of CO_2. *Catal. Commun.* **2007**, *8*, 1317–1322. [CrossRef]
42. Zhang, X.; Ye, Q.; Xu, B.; He, D. Oxidative dehydrogenation of ethane over Co–$BaCO_3$ catalysts using CO_2 as oxidant: Effects of Co promoter. *Catal. Lett.* **2007**, *117*, 140–145. [CrossRef]

43. Elkabouss, K.; Kacimi, M.; Ziyad, M.; Ammar, S.; Bozon-Verduraz, F. Cobalt-exchanged hydroxyapatite catalysts: Magnetic studies, spectroscopic investigations, performance in 2-butanol and ethane oxidative dehydrogenations. *J. Catal.* **2004**, *226*, 16–24. [CrossRef]
44. Myint, M.; Yan, B.; Wan, J.; Zhao, S.; Chen, J.G. Reforming and oxidative dehydrogenation of ethane with CO_2 as a soft oxidant over bimetallic catalysts. *J. Catal.* **2016**, *343*, 168–177. [CrossRef]
45. Zhang, X.; Zhu, A.; Li, X.; Gong, W. Oxidative dehydrogenation of ethane with CO_2 over catalyst under pulse corona plasma. *Catal. Today* **2004**, *89*, 97–102. [CrossRef]
46. Peng, X.; Zhu, J.; Yao, L.; Hu, C. Effect of methane co-feeding on the selectivity of ethylene produced from oxidative dehydrogenation of ethane with CO_2 over a Ni-La/SiO_2 catalyst. *J. Energy Chem.* **2013**, *22*, 653–658. [CrossRef]
47. Xu, L.; Liu, J.; Yang, H.; Xu, Y.; Wang, Q.; Lin, L. Regeneration behaviors of Fe/SiO_2 and Fe–Mn/SiO_2 catalysts for C_2H_6 dehydrogenation with CO_2 to C_2H_4. *Catal. Lett.* **1999**, *62*, 185–189. [CrossRef]
48. Nakagawa, K.; Kajita, C.; Ikenaga, N.-O.; Nishitani-Gamo, M.; Ando, T.; Suzuki, T. Dehydrogenation of light alkanes over oxidized diamond-supported catalysts in the presence of carbon dioxide. *Catal. Today* **2003**, *84*, 149–157. [CrossRef]
49. Ogonowski, J.; Skrzyńska, E. Conversion of Lower Hydrocarbons in the Presence of Carbon Dioxide: The Theoretic Analysis and Catalytic Tests over Active Carbon Supported Vanadium Oxide. *Catal. Lett.* **2008**, *124*, 52–58. [CrossRef]
50. Qiao, A.; Kalevaru, V.N.; Radnik, J.; Martin, A. Oxidative dehydrogenation of ethane to ethylene over Ni–Nb–M–O catalysts: Effect of promoter metal and CO_2-admixture on the performance. *Catal. Today* **2016**, *264*, 144–151. [CrossRef]
51. Solymosi, F.; Németh, R. The oxidative dehydrogenation of ethane with CO_2 over Mo_2C/SiO_2 catalyst. *Catal. Lett.* **1999**, *62*, 197–200. [CrossRef]
52. Chen, M.; Xu, J.; Liu, Y.-M.; Cao, Y.; He, H.-Y.; Zhuang, J.-H. Supported indium oxide as novel efficient catalysts for dehydrogenation of propane with carbon dioxide. *Appl. Catal. A* **2010**, *377*, 35–41. [CrossRef]
53. Zhu, J.; Qin, S.; Ren, S.; Peng, X.; Tong, D.; Hu, C. Na_2WO_4/Mn/SiO_2 catalyst for oxidative dehydrogenation of ethane using CO_2 as oxidant. *Catal. Today* **2009**, *148*, 310–315. [CrossRef]
54. Wu, R.; Xie, P.; Cheng, Y.; Yue, Y.; Gu, S.; Yang, W.; Miao, C.; Hua, W.; Gao, Z. Hydrothermally prepared Cr_2O_3–ZrO_2 as a novel efficient catalyst for dehydrogenation of propane with CO_2. *Catal. Commun.* **2013**, *39*, 20–23. [CrossRef]
55. Hakuli, A.; Harlin, M.E.; Backman, L.B.; Krause, A.O.I. Dehydrogenation of i-Butane on CrO_x/SiO_2 Catalysts. *J. Catal.* **1999**, *184*, 349–356. [CrossRef]
56. Wang, G.; Zhang, L.; Deng, J.; Dai, H.; He, H.; Au, C.T. Preparation, characterization, and catalytic activity of chromia supported on SBA-15 for the oxidative dehydrogenation of isobutane. *Appl. Catal. A* **2009**, *355*, 192–201. [CrossRef]
57. Kim, D.S.; Tatibouet, J.-M.; Wachs, I.E. Surface structure and reactivity of CrO_3/SiO_2 catalysts. *J. Catal.* **1992**, *136*, 209–221. [CrossRef]
58. Baek, J.; Yun, H.J.; Yun, D.; Choi, Y.; Yi, J. Preparation of Highly Dispersed Chromium Oxide Catalysts Supported on Mesoporous Silica for the Oxidative Dehydrogenation of Propane Using CO_2: Insight into the Nature of Catalytically Active Chromium Sites. *ACS Catal.* **2012**, *2*, 1893–1903. [CrossRef]
59. Puurunen, R.L.; Weckhuysen, B.M. Spectroscopic Study on the Irreversible Deactivation of Chromia/Alumina Dehydrogenation Catalysts. *J. Catal.* **2002**, *210*, 418–430. [CrossRef]
60. Cecilia, J.A.; García-Sancho, C.; Mérida-Robles, J.M.; Santamaría-González, J.; Moreno-Tost, R.; Maireles-Torres, P. V and V–P containing Zr-SBA-15 catalysts for dehydration of glycerol to acrolein. *Catal. Today* **2015**, *254*, 43–52. [CrossRef]
61. Klimova, T.; Gutiérrez, O.; Lizama, L.; Amezcua, J. Advantages of ZrO_2- and TiO_2–SBA-15 mesostructured supports for hydrodesulfurization catalysts over pure TiO_2, ZrO_2 and SBA-15. *Microporous Mesoporous Mater.* **2010**, *133*, 91–99. [CrossRef]
62. Lizama, L.; Amezcua, J.C.; Klimova, T. Development of New Hybrid TiO_2/SBA-15 Mesoporous Molecular Sieves and Their Use as Supports for Deep Hydrodesulfurization NiMo Catalysts. In *Studies in Surface Science and Catalysis*; Gédéon, A., Massiani, P., Babonneau, F., Eds.; Elsevier: Amsterdam, The Netherlands, 2008; Volume 174, pp. 1351–1354.

63. Zhao, X.; Wang, X. Oxidative dehydrogenation of ethane to ethylene by carbon dioxide over Cr/TS-1 catalysts. *Catal. Commun.* **2006**, *7*, 633–638. [CrossRef]
64. Al-Awadi, A.S.; El-Toni, A.M.; Al-Zahrani, S.M.; Abasaeed, A.E.; Alhoshan, M.; Khan, A.; Labis, J.P.; Al-Fatesh, A. Role of TiO_2 nanoparticle modification of Cr/MCM41 catalyst to enhance Cr-support interaction for oxidative dehydrogenation of ethane with carbon dioxide. *Appl. Catal. A* **2019**, *584*, 117114. [CrossRef]
65. Bai, P.T.; Srinath, S.; Upendar, K.; Sagar, T.V.; Lingaiah, N.; Rao, K.R.; Prasad, P.S. Oxidative dehydrogenation of ethane with carbon dioxide over Cr_2O_3/SBA-15 catalysts: The influence of sulfate modification of the support. *Appl. Petrochem. Res.* **2017**, *7*, 107–118.
66. Jehng, J.-M.; Wachs, I.E.; Weckhuysen, B.M.; Schoonheydt, R.A. Surface chemistry of silica–titania-supported chromium oxide catalysts. *J. Chem. Soc. Faraday Trans.* **1995**, *91*, 953–961. [CrossRef]
67. Al-Awadi, A.S.; Al-Zahrani, S.M.; El-Toni, A.M.; Abasaeed, A.E. Dehydrogenation of Ethane to Ethylene by CO_2 over Highly Dispersed Cr on Large-Pore Mesoporous Silica Catalysts. *Catalysts* **2020**, *10*, 97. [CrossRef]
68. Moulder, J.F. *Handbook of X-ray Photoelectron Spectroscopy*; Physical Electronics: Eden Prairie, MN, USA, 1995; pp. 230–232.
69. Wu, D.; Ma, J.; Bao, Y.; Cui, W.; Hu, T.; Yang, J.; Bai, Y. Fabrication of Porous Ag/TiO_2/Au Coatings with Excellent Multipactor Suppression. *Sci. Rep.* **2017**, *7*, 43749. [CrossRef]
70. Yurddaskal, M.; Dikici, T.; Yildirim, S.; Yurddaskal, M.; Toparli, M.; Celik, E. Fabrication and characterization of nanostructured anatase TiO_2 films prepared by electrochemical anodization and their photocatalytic properties. *J. Alloys Compd.* **2015**, *651*, 59–71. [CrossRef]
71. Ayari, F.; Mhamdi, M.; Álvarez-Rodríguez, J.; Ruiz, A.R.G.; Delahay, G.; Ghorbel, A. Selective catalytic reduction of NO with NH_3 over Cr-ZSM-5 catalysts: General characterization and catalysts screening. *Appl. Catal. B Environ.* **2013**, *134*, 367–380. [CrossRef]
72. Michorczyk, P.; Ogonowski, J.; Zeńczak, K. Activity of chromium oxide deposited on different silica supports in the dehydrogenation of propane with CO_2—A comparative study. *J. Mol. Catal. A Chem.* **2011**, *349*, 1–12. [CrossRef]
73. Cavani, F.; Koutyrev, M.; Trifirò, F.; Bartolini, A.; Ghisletti, D.; Iezzi, R.; Santucci, A.; Del Piero, G. Chemical and Physical Characterization of Alumina-Supported Chromia-Based Catalysts and Their Activity in Dehydrogenation of Isobutane. *J. Catal.* **1996**, *158*, 236–250. [CrossRef]
74. Weckhuysen, B.M.; Wachs, I.E.; Schoonheydt, R.A. Surface Chemistry and Spectroscopy of Chromium in Inorganic Oxides. *Chem. Rev.* **1996**, *96*, 3327–3350. [CrossRef]
75. Rao, T.V.M.; Yang, Y.; Sayari, A. Ethane dehydrogenation over pore-expanded mesoporous silica supported chromium oxide: 1. Catalysts preparation and characterization. *J. Mol. Catal. A Chem.* **2009**, *301*, 152–158. [CrossRef]
76. Sun, B.; Reddy, E.P.; Smirniotis, P.G. Effect of the Cr^{6+} concentration in Cr-incorporated TiO_2-loaded MCM-41 catalysts for visible light photocatalysis. *Appl. Catal. B Environ.* **2005**, *57*, 139–149. [CrossRef]
77. Sun, B.; Reddy, E.P.; Smirniotis, P.G. TiO_2-loaded Cr-modified molecular sieves for 4-chlorophenol photodegradation under visible light. *J. Catal.* **2006**, *237*, 314–321. [CrossRef]